ELSEVIER

Contents lists available at ScienceDirect

Journal of the European Ceramic Society

journal homepage: www.elsevier.com/locate/jeurceramsoc



Original Article

Comparing hydrothermal sintering and cold sintering process: Mechanisms, microstructure, kinetics and chemistry



Arnaud Ndayishimiye^{a,b,*,1}, Mert Y. Sengul^{a,b,1}, Sun Hwi Bang^{a,b}, Kosuke Tsuji^{a,b}, Kenji Takashima^{a,c}, Thomas Hérisson de Beauvoir^d, Dominique Denux^e, Jean-Marc Thibaud^e, Adri C.T. van Duin^{a,b,f}, Catherine Elissalde^e, Graziella Goglio^e, Clive A. Randall^{a,b}

- ^a Materials Research Institute, The Pennsylvania State University, University Park, PA 16802, United States
- b Department of Materials Science and Engineering, The Pennsylvania State University, University Park, PA 16802, United States
- c TAIYO YUDEN CO., LTD., Kyobashi, Chuo-ku, Tokyo 104-0031, Japan
- d CIRIMAT, Université de Toulouse, CNRS, Université de Toulouse 3 Paul Sabatier, 118 Route de Narbonne 31062, Toulouse, Cedex 9, France
- e CNRS, Université de Bordeaux, ICMCB, UMR 5026, 87 Avenue du Dr A. Schweitzer, 33608, Pessac, France
- f Department of Mechanical Engineering, The Pennsylvania State University, University Park, PA 16802, United States

ARTICLE INFO

Keywords: Hydrothermal sintering Cold sintering Ceramics ReaxFF Molecular dynamics

ABSTRACT

This study reports the sintering of zinc oxide (ZnO) through the comparison between the hydrothermal sintering (HS) and the cold sintering process (CSP) operating in closed and open conditions, respectively. Sintering was performed at 155 \pm 5 °C applying a pressure of 320 MPa, and during different holding times (0 min, 20 min, 40 min and 80 min). Whatever the low sintering process used, ceramics characteristics are almost similar in terms of relative densities and ZnO structure. However, several differences such as the nature of stabilized phases, grain sizes and quantities of residual molecules in the densified pellets, were characterized and explained. The formation of zinc acetate "bridges" was observed *ex situ* in hydrothermally sintered samples. A detailed ReaxFF molecular dynamics simulation was performed to help understand the formation mechanisms of zinc acetate "bridges" and compare the chemical activities between HS and CSP.

1. Introduction

Currently, research is directed towards materials with new properties, improved performance to cost ratio and limited environmental impact over their entire life cycle. Ceramics and ceramic-based composites are enabling materials that are highly investigated as their use cover multiple applications in fields such as energy storage, electronics, aeronautics and aerospace among others. Most of the methods to densify ceramic materials require the use of temperatures above 1000 °C, to reach at least 95 % of relative densities. However, these high processing temperatures come with their own drawbacks such as low energy efficiency, non-suitability for metastable materials or materials with low decomposition temperatures, interdiffusion leading for unsought interphases during the co-sintering of multimaterials.

Nowadays, there is a growing interest to develop low temperature sintering processes (T $<400\,^{\circ}\text{C})$ to overcome these technological limitations associated with high temperature processing methods. These last decades, there have been a few important contributions to sintering

at low temperatures with these processes operating in open or closed systems (Fig. 1)

1.1. Closed systems

Early investigations on low temperature densification of materials were conducted on closed systems. In the early 70's, D.M. Roy et al. prepared, at Penn State University, cement pastes with excellent mechanical properties and almost no porosity by hot pressing Cementous powders and water [1,2]. In the mid-70's, further studies were made by S. Sōmiya et al. on reactive hydrothermal sintering to obtain densified oxides, starting from metal powders at temperatures higher than 900 °C [3,4]. In combining both these approaches, N. Yamasaki, K. Yanagisawa et al. from Kochi University developed an apparatus for "hydrothermal hot pressing", based in uniaxial pressure of a mixture of powder and solvent in a system sealed with PTFE (Teflon Topowder and solvent in a system sealed with PTFE (Teflon Topowder such as SiO₂, TiO₂, hydroxyapatite, CaCO₃, Ca₃CO₄O₉, zeolites,

^{*} Corresponding author at: Materials Research Institute, The Pennsylvania State University, University Park, PA 16802, United States. E-mail address: axn536@psu.edu (A. Ndayishimiye).

 $^{^{1}}$ These authors have contributed equally to this work.

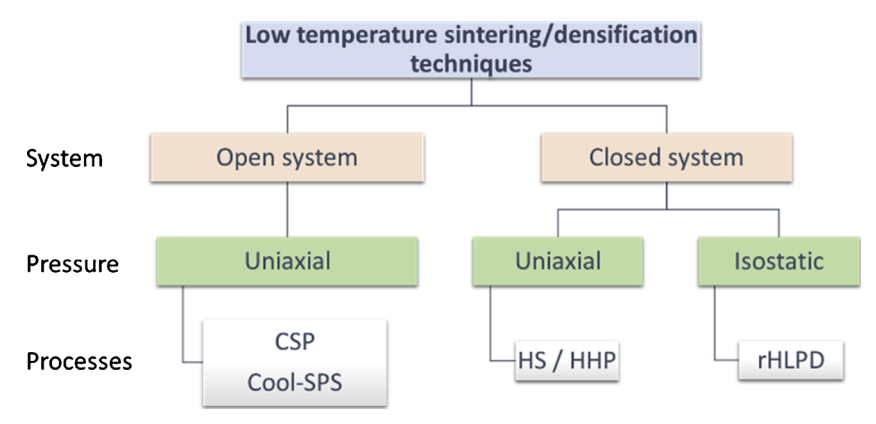


Fig. 1. Different low temperature sintering and densification methods. CSP: Cold Sintering Process, Cool-SPS: Cool Spark Plasma Sintering, HS: Hydrothermal Sintering, HHP: Hydrothermal Hot Pressing, rHLPD: reactive Hydrothermal Liquid Phase Densification.

Sn $_{1.24}$ Ti $_{1.94}$ O $_{3.66}$ (OH) $_{1.50}$ F $_{1.42}$ [6–10]. However, except hydroxyapatite and Sn $_{1.24}$ Ti $_{1.94}$ O $_{3.66}$ (OH) $_{1.50}$ F $_{1.42}$, most of the materials had relative densities lower than 80 %. This technique was further developed and renamed "hydrothermal sintering" by Goglio et al. at the University of Bordeaux. A high-performance apparatus was designed to reach higher temperatures and pressures while keeping gaskets out of the hot zone and maintain the system hermetically sealed [11,12]. With this technique, quasi-complete densification of α -quartz was made as well as silica-based composites [13–15].

Recently, Riman et al. at Rutgers University developed the "Reactive Hydrothermal Liquid Phase Densification (rHLPD) [16]. In this technique, a porous preform is infiltrated with precursors and submitted to isostatic pressure and mild temperatures. Then, hydrothermal reactions between the preform and precursors take place, leading to reactive crystallization and densification of the material. This technique allowed to densify ceramics and composites such as BaTiO $_3$, SrTiO $_3$, Ca(PO $_4$)F $_2$, Sr(PO $_4$)(OH) $_2$, CaCO $_3$ /SiO $_2$ with relative densities up to 90 % at temperatures below 400 °C and at times up to 72 h [17,18].

1.2. Open systems

Investigations on open systems are more recent. The cold sintering process, developed at Penn State University by Randall et al. operates in an open system, with non-equilibrium conditions [19–21]. The pressure is applied uniaxially on a powder mixed with a solvent and the densification is mainly driven by a pressure solution creep mechanism [22]. The cold sintering process enabled the sintering of several ceramics such as LiMoO₄, BaTiO₃, ZnO, Li_{1.5}Al_{0.5}Ge_{1.5}(PO₄)₃, V₂O₅ and many other bulk and multilayer composites [23–26]. One of the other major breakthroughs of cold sintering is that the technique enabled the fabrication of ceramic-polymer composites with a high volume fraction of ceramics (up to 99.9 %), that were initially impossible to obtain due to temperature gaps between elevated temperatures conventionally necessary to sinter ceramics and decomposition temperatures of polymers [27].

Among other low temperature sintering techniques, Cool-SPS was used to densify thermodynamically fragile materials, including reactive sintering of hydrated precursors at temperatures below 400 $^{\circ}$ C [28–30].

ZnO is of particular interest in the material science community due to its earth-abundance, low price, tunable surface chemistry through defects, appealing physical properties for a wide range of applications in semiconductor electrochemistry, photochemistry and catalysis [31]. Because nanometric ZnO exhibits a high surface reactivity, good affinity with solvents, a great diversity of grain morphologies and a congruent dissolution, it establishes itself as a particularly suitable material for low sintering process.

ZnO was first cold sintered by Funahashi et al. [32]. Among solvents

tested in this study, acetic acid provided the best results as it let to relative densities of 98 %, electrical conductivities equivalent to conventionally sintered materials and an activation energy for grain growth of 43 KJ. mol^{-1} , which is at least five times lower than the one in conventional sintering [33,34]. Guillon et al. also sintered ZnO in the presence of a small amount of water (1.7 wt. %) using FAST/SPS apparatus. High relative densities were obtained, and authors proposed that the main effects of adsorbed water were a better initial packing due to reduction of interparticle friction, dissolution of Zn^{2+} and O^{2-} ions on the surface particle, defect formation due to diffusion of H^+ and OH^- ions into the ZnO crystals, formation of a highly defective diffusion path between grains and carbonate elimination. All these effects would then be amplified by acetates [35]. Recently some attempts to experimentally become closer to the conditions of a closed system were made by Kang et al. [36].

In this paper, we propose a direct comparison between the cold sintering process (CSP) and the hydrothermal sintering (HS) focused on zinc oxide (ZnO). The complementary use of these two processes offers a unique opportunity to decipher the complex kinetics and thermodynamics of chemical reactions involved in the densification mechanism. Materials were sintered at 155 \pm 5 °C with a uniaxial pressure of 320 MPa, and different dwell times (0, 20, 40 and 80 min). The obtained ceramics were then thoroughly characterized, which has revealed that mechanical chemical effects are common densification driving force, but the chemical pathways depend on the sintering process. In particular, the formation of zinc acetate "bridges" observed specifically in hydrothermally-sintered specimen was modelled by Reactive Force Field Molecular Dynamics (ReaxFF MD).

2. Experimental Section

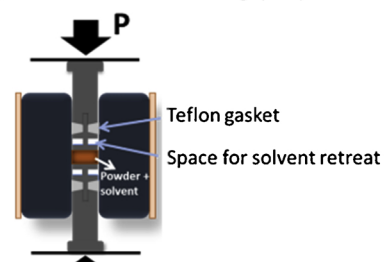
2.1. Powder preparation

ZnO (99.9 %, Alfa Aesar), with particle size of 40-100 nm, was used as starting powder. A 2 M solution of acetic acid was prepared from the dilution of glacial acetic acid (VWR, 17.6 M, VW0125-3).

2.2. Cold sintering and hydrothermal sintering experiments

For each sample, 1 g of ZnO powder was mixed with 15 wt. % of 2 M of acetic acid. Powder and solvent were manually mixed with an agate mortar and pestle for 2 min. The mixture was then poured into a: a) $10.0 \, \text{mm}$ diameter Inconel die with pistons equipped with a Teflon gasket in order to maintain the system closed for the hydrothermal sintering (Fig. 2a), or into a b) $12.7 \, \text{mm}$ diameter stainless steel die and uniaxially pressed using a Carver Model M press for the cold sintering (Fig. 2b). In both cases, the mixture was first pressed under $320 \, \text{MPa}$ at room temperature for $10 \, \text{min}$ to allow further particle rearrangement,

(a) Hydrothermal Sintering (HS)



(b) Cold Sintering Process (CSP)

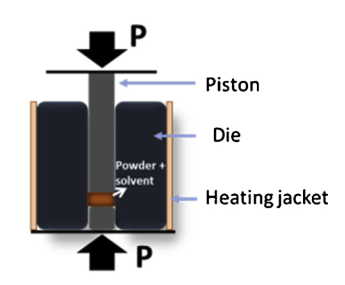


Fig. 2. Simplified schematics to highlight main differences between (a) Hydrothermal sintering, (b) Cold sintering and their main specificities. Fig. S1 in Supplementary Data shows more detailed schematics.

Table 1
Names of ZnO samples prepared by hydrothermal sintering (HS) and cold sintering (CSP) with different dwell times.

Dwell Tech.	0 min	20 min	40 min	80 min
HS	HS0	HS20	HS40	HS80
CSP	CSP0	CSP20	CSP40	CSP80

then the temperature was increased to $155\,^{\circ}\text{C}$ with a $10\,^{\circ}\text{C.min}^{-1}$ heating rate average. The mixture was then maintained in the die at $155\,\pm\,5\,^{\circ}\text{C}$ for different dwell times (0, 20, 40 and 80 min) and the pressure was constantly readjusted when shrinkage was observed. At the end of the dwell, the pressure was naturally released as the system was cooling down to room temperature. Names of as-produced pellets are specified in Table 1.

2.3. Material characterization

2.3.1. X-ray diffraction (XRD)

Crystalline phases in the sintered pellets were characterized by X-ray diffraction (XRD) with a PANalytical Empyrean diffractometer, operating at 45 kV and 40 mA. Diffraction signals were collected between 20 angles of 5° and 70° , using a step size of 0.026° with a Cu K α radiation. Diffractograms were refined with the software Fullprof [37].

2.3.2. Density measurements

Real densities ($\rho_{\rm real}$) of CSP and HS pellets were measured by He gas pycnometer (Micromeritics Accupyc II 1340), using an equilibration pressure of 0.0050 psig min $^{-1}$ for high precision measurements. Bulk densities ($\rho_{\rm bulk}$) were obtained by the Archimedes method, using ethanol as the liquid medium. The mass of the as-produced sample (m_d) was first measured. Then the sample was immersed in ethanol for 2 min to fill open pores with the fluid, prior to measuring the mass of the sample in the liquid medium (m_1). The sample surface was then gently wiped to remove any excess on the surface and the mass of the sample saturated with liquid (m_s) was measured in air.

The bulk density was calculated by the following relation:

$$\rho \text{bulk} = \frac{m_d. \, \rho_{fluid}}{(m_s - m_l)}$$

The relative density ($d_{\rm rel.}$) was then calculated with the following relation:

$$d_{rel.} = \frac{\rho_{bulk}}{\rho_{out}}$$

2.3.3. High resolution scanning Electron microscopy (HR - SEM)

High Resolution Scanning Electron Microscopy (HR - SEM) was performed on a FEI Nova NanoSEM 630, with accelerating voltages of

7 kV. Analysis were made on iridium-sputtered fractures at the center of ceramics. The grain size measurement was performed with the freeware Image J [38] on a population of 180 grains.

2.3.4. High resolution transmission electron microscopy

Samples for transmission electron microscopy (TEM) analysis were prepared using a FEI Helios 660 focused ion beam (FIB) system. A thick protective amorphous carbon layer was deposited over the region of interest then Ga⁺ ions (30 kV then stepped down to 1 kV to avoid ion beam damage to the sample surface) were used in the FIB to make the samples electron transparent for TEM images. A FEI Titan G2 (60–300 kV) electron microscope equipped with a superX EDS system was used, with an accelerating voltage of 300 kV for high resolution imaging (HR-TEM), high angle annular dark field (HAADF) scanning transmission microscope (STEM) and energy dispersive spectroscopy (EDS) mapping.

2.3.5. Thermal gravimetric analysis and mass spectroscopy (TG-MS)

Thermal gravimetric analysis and mass spectroscopy (TGA-MS) were performed between 20 and 600 °C under an argon gas (Ar) flow, with a heating ramp of 10 °C.min $^{-1}$ using a SETARAM TAG 2400 equipment coupled with a BALZER THERMOSTAR mass spectrometer. Non-crushed pieces of sintered samples with a mass of 25.0 \pm 0.1 mg were used.

2.3.6. Raman spectroscopy

Raman spectroscopy was carried out at room temperature with a Horiba Scientific confocal Raman system (LabRAM HR Evolution) with 488 nm laser at a power level of 1.5 mW. The acquisition time was 10 s and the spectra were accumulated twice to increase the signal/noise ratio. Raman spectra presented in this study were taken under the exact same conditions and different points to ensure a rigorous comparison.

2.3.7. ReaxFF analysis

The zinc (Zn) atoms are tetrahedrally coordinated by oxygen (O) atoms in wurtzite structure. The wurtzite ($10\overline{1}0$) surface is a low-index surface [39,40]. Each surface Zn cation is missing an O anion, and each surface O anion is missing the nearest zinc cation. The simulated ZnO slab was composed of 14 layers with a thickness of more than the cutoff value of the interactions between atoms. The total number of atoms in the slab was 3528. The number of Zn²⁺ ions in the solvent phase was 100, and 50 water molecules and two acetate molecules were placed for each Zn²⁺ ion, which corresponds to a total number of atoms of 16500 in the solvent phase. The acetic acid, water and Zn²⁺ mixtures were prepared by positioning each molecule randomly into the simulation box. The density of the mixtures was calculated by taking water density as 1 g/cm³ and acetic acid density as 1.05 g/cm³. The final density was achieved by adjusting the simulation box dimensions accordingly. The prepared equilibrated solvent slabs were placed on the ZnO surface and equilibrated at 300 K. In order to model the gaseous solvent state in

Cold Sintering Process (CSP), the simulation box dimensions were enlarged in the direction perpendicular to the surface to create a vacuum region and equilibrated while maintaining the liquid state density of solvent. Both CSP and Hydrothermal Sintering (HS) simulation boxes were heated slowly to 500 K with an increment of 0.002 K/fs. The ReaxFF potential that was used in this study was developed to model ZnO $(10\overline{1}0)$ /acetic acid/water interfacial interactions [41]. The potential was also reoptimized to make it capable of modeling sub and supercritical conditions in acetic acid-water mixtures [42]. The ReaxFF MD calculations were performed using the ADF software [43]. A time step of 0.25 fs was used to integrate the Newtonian equations of motion by using a velocity-Verlet algorithm. A weak Berendsen thermostat [44] was used to control the simulation box temperatures at desired values. The temperature-damping constant used for the thermostat was 0.1 ps. In order to increase the simulation timescale to investigate the clustering in hydrothermal conditions, the surface was removed from the system, and the solvent phase was simulated for 1 ns. The clustering simulation systems were composed of 100 Zn²⁺ ions, 200 acetate ions and 6200 water molecules which corresponds to a total of 20100 atoms.

3. Results

3.1. Sintering of ZnO

Fig. 3 shows the relative density evolution of ZnO ceramics as a function of CSP and HS dwell time. In both cases, very high relative densities (> 98 %) can be already achieved with a dwell time of 0 min. The difference in relative density between the two processes is less than 2 %. For both the cold sintering and hydrothermal sintering, the evolution of the relative density with time is nonlinear as a decrease followed by an increase in the density after dwell times of 20 and 40 min is observed for cold sintering and hydrothermal sintering, respectively.

3.2. Structural and microstructural characterization of hydrothermally- and cold-sintered ZnO

XRD patterns of cold sintered samples are single phased ZnO (Fig. 4b), with the crystallographic cell parameters (Supplementary Data, Table S1) obtained after Rietveld refinement (Supplementary Data, Fig. S 2) are in agreement with the values reported in the literature (a = 3.249(1) Å and c = 5.206(1) Å, space group: P6₃mc) [45]. The ratio c/a is 1.602, a value smaller than the theoretical one expected for an undistorted Wurtzite structure c/a = 8/3 = 1.633 [46]. The main phase of hydrothermally sintered samples is also ZnO (Fig. 4a) with similar crystallographic cell parameters. However, a low intensity

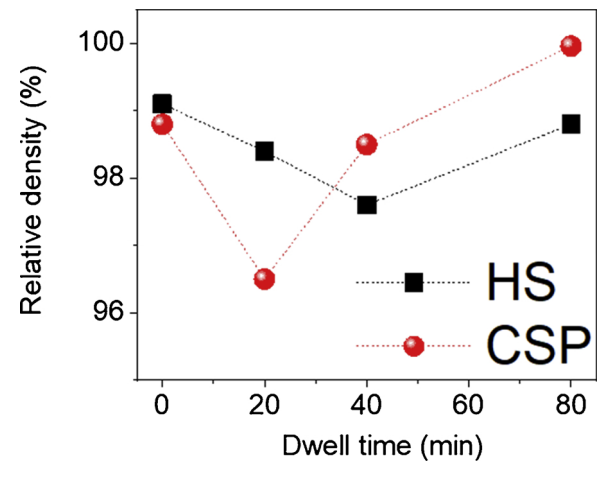


Fig. 3. Relative density of ZnO hydrothermally- and cold-sintered at 155 \pm 5 °C, with different dwell times. Dash lines must be considered as guide-to-the-eye.

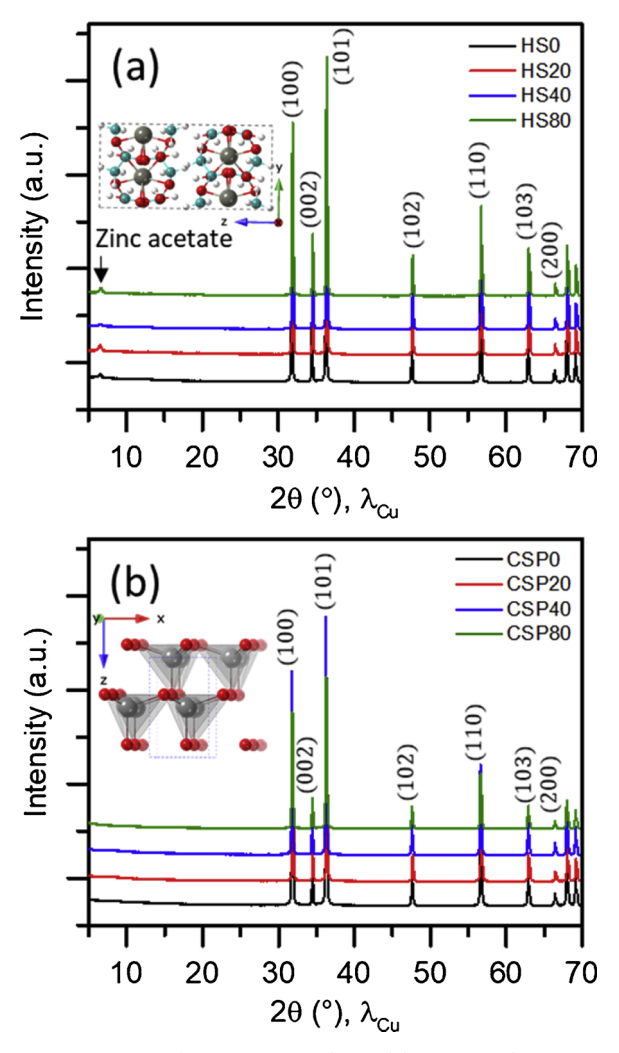


Fig. 4. XRD patterns of ZnO ceramics obtained by (a) HS, (b) CSP. Crystal structures of zinc acetate dihydrate and zinc oxide (wurtzite) are presented in insets of (a) and (b), respectively. Key: Zn atom (grey), Oxygen atom (red), Hydrogen atom (white), Carbon atom (cyan). (For interpretation of the references to colour in this figure legend, the reader is referred to the web version of this article).

diffraction peak at $20 \sim 6.5^{\circ}$ consistent with the presence of crystalline zinc acetate [47,48] is observed whatever the dwell time (Fig. 4a).

Vibrational properties of ZnO were studies by Raman spectroscopy (Fig. 5). At the center of the Brillouin point Γ , phonons resulting from the Stokes Raman scattering of laser photons (with a wavelength λ) in interaction with a P6₃mc ZnO, are represented by symmetry modes: $\Gamma = A_1 + E_1 + 2B_1 + 2E_2$.

 A_1 and E_1 modes are both polar and split into a transverse optical mode (TO) and a longitudinal optical mode (LO). E_2 mode consists of low and high frequency phonon noted E_2 (low) and E_2 (high), respectively. The mode E_2 (high) is associated with the vibration of oxygen atoms, while E_2 (low) is related to heavy Zn sublattices. E_1 is a Raman silent mode [49].

The vibrational activity of the mode $E_1(LO)$, derived from the formation of oxygen vacancies [50], is observed with a broaden peak centered at 577 - 585 cm⁻¹ and probably overlaps with the $A_1(LO)$ mode only when the c-axis of wurtzite ZnO is parallel to the sample surface [51]. A_1 (TO) and E_1 (TO) modes were observed at 380 and 412 cm⁻¹, respectively. The vibrational activity of the E_2 (TO) - E_2 (LO) mode was observed at 332 cm⁻¹. The E_2 modes at low and high frequency are respectively at 98 and 437 cm⁻¹.

The bands at ~ 1105 and 1155 cm⁻¹ can be attributed to 2 A₁(LO)

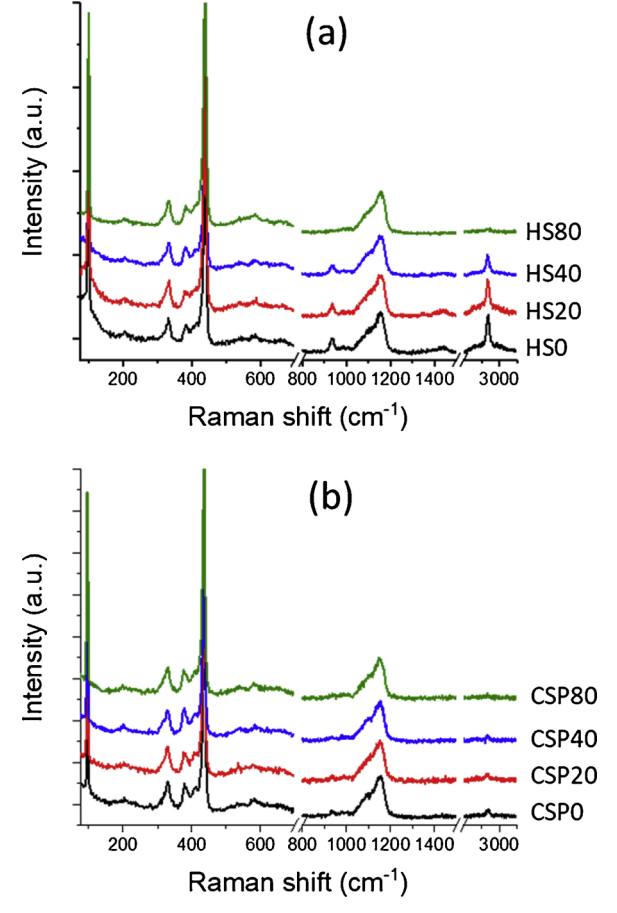


Fig. 5. Raman spectroscopy of ZnO ceramics obtained by (a) HS and (b) CSP.

scattering at points H and K, and the convolution of 2 $A_1(LO)$ and $2E_1(LO)$ modes at the point Γ of the Brillouin zone, respectively [52]. Besides ZnO-related vibrations, we observe additional bands located at 938, 1426 and 2935 cm $^{-1}$, attributed to C–C, C–O and CH $_3$ symmetric stretching, respectively [53].

Prior to analyses, Raman spectra of both cold and hydrothermally-sintered samples were normalized with the asymmetric LO multiphonon peak located at 1155 cm⁻¹ as reference (Fig. 5). No significant changes are observed, except for the peaks located at 938, 1426 and 2935 cm⁻¹, respectively attributed to C–C, C–O and CH₃ symmetric stretching.

For hydrothermal sintering, intensities of bands attributed to C–C, C–O and CH_3 symmetric stretching progressively decrease with the sintering time, up to extremely low values for the sample HS80. For the cold sintering process, only a very low intensity band attributed to CH_3 symmetric stretching is clearly visible. The intensity further decreases with the sintering time until quasi-full disappearance for the sample CSP80.

Fig. 6 shows SEM images of ZnO hydrothermally- and cold-sintered at 155 \pm 5 °C with dwell times ranging between 0 and 80 min. In all cases, necking and grain growth are obvious as grains are cohesive, with sizes higher than the initial particles (40–100 nm). The evolution of grain size dwell versus time presented in Fig. 6 insets and Fig. 7 depends on the process. In the case of HS, the grain size increases from 166 \pm 55 to 229 \pm 70 nm, reaching a plateau from \sim 40 min (HS40). It is interesting to notice that despite this constant size, the relative density increases. In the case of CSP, the grain size continuously increases as a function of time from 131 \pm 42 to 334 \pm 117 nm. Moreover, this evolution of the grain size distribution versus sintering time is also interesting as it highlights the decrease in the number of small grains at the advantage of larger grains. As a conclusion, despite

close values of relative densities, the microstructures show some significant differences depending on the sintering process, highlighting an equilibrium state reached in the case of HS from 40 min dwell time, while the system continuously evolves in the case of CSP. The evolution of grain size distribution may reflect grain growth following an Ostwald ripening-type of mechanism and/or a coalescence phenomenon.

We also observe in SEM the presence of zinc acetate "bridges" after hydrothermal sintering, but not after cold sintering. These results are consistent with XRD analysis and Raman spectroscopy analysis (Figs. 4 and 5). The formation of zinc acetate "bridges" can be exacerbated with the sintering temperature (Supplementary Data, Fig. S 3). It is important to note that samples were not polished to avoid damages these "acetate bridges" (Supplementary Data, Fig. S 4).

3.3. Thermal decomposition of ZnO ceramics prepared by HS and CSP

To access and quantify the residual organics further, the thermal decomposition of cold sintered and hydrothermally sintered samples was studied by TGA (Fig. 8a-d). In our low sintering temperature conditions, TGA reveals total mass losses within the range of 1.24-2.59 % and 0.45 – 0.65 % for hydrothermal and cold sintering, respectively. Hydrothermally-sintered samples systematically show higher mass losses than cold-sintered samples. TG-MS was used to thoroughly and qualitatively evaluate evolved gas molecules during heating. For sake of clarity, only MS data of samples prepared with a 40 min dwell time will be highlighted. Indeed, only quantitative differences and no significant qualitative differences are noticed between CSP and HS samples (Supplementary Data, Fig. S 5). For both hydrothermally- and cold-sintered samples, Mass Spectroscopy analysis (Fig. 8e and f) reveals that mass losses below 150 °C are mainly due to water, as ions at m/z 17 and 18 that respectively correspond to OH and H_2O fragments are detected. The water may come from the adsorption of ambient humidity [54,55], residual H2O used to prepare the solvent as well as the releasing of water molecules to form anhydrous zinc acetate $Zn(CH_3CO_2)_2$ and acetic acid CH3COOH, following the thermal decomposition of CH_3COOH . xH_2O and $Zn(CH_3CO_2)_2$. xH_2O , respectively.

In the temperature region between 120 and ~ 280 °C, mass spectra show the release of ions at m/z 15, 17, 18, 30, 43, 44 and 60, which correspond to CH_3 , HO, H_2O , CH_2O , CH_3CO , CO_2 and CH_3COOH fragments, respectively. In highly humid atmospheres, anhydrous zinc acetate reacts to spontaneously form ZnO and acetic acid following the Eq. (1): [56]

$$Zn(CH_3CO_2)_2 + H_2 O \rightarrow ZnO + 2CH_3COOH$$
 (1)

Acetic acid resulting from this latter decomposition as well as the one originating from the residual solvent, then decomposes following different schemes, as evidenced by the variety of obtained fragments. Sengul et al. [41] highlighted by ReaxFF molecular dynamics that acetic acid molecules in interaction with ZnO surfaces can form formaldehyde (CH_2O) and carbon dioxide (CO_2), following the sequence presented in Eqs. (2a) and (2b):

$$CH_3COO_{(ad)} + HO_{(ad)} \rightarrow COH_2COO_{(ad)} + 2H_{(ad)}$$
 (2a)

$$COH_2COO_{(ad)} \rightarrow CH_2O + CO_2$$
 (2b)

Yoneyama et al. have shown that the interaction between acetate ions and holes (h^+) in inorganic materials can form methyl radical (CH_3^-) and carbon dioxide (CO_2) (Eq. (3)). Besides, the reaction between an OH radical with anhydrous acetic acid leads to the formation of water (H_2O) , CO_2 and CH_3^- (Eq. (4)). [57] Reaction at Eq. (4) more likely takes place at $\sim 237\,^{\circ}\text{C}$ as we simultaneously observe an increase in the release of these three latter molecules.

$$CH_3COO^- + h^+ \rightarrow CH_3 + CO_2 \tag{3}$$

$$CH_3COOH + HO \rightarrow CH_3 + CO_2 + H_2O$$
 (4)

From ~ 200 °C, we also observe the release of ions at m/z 58, 59,

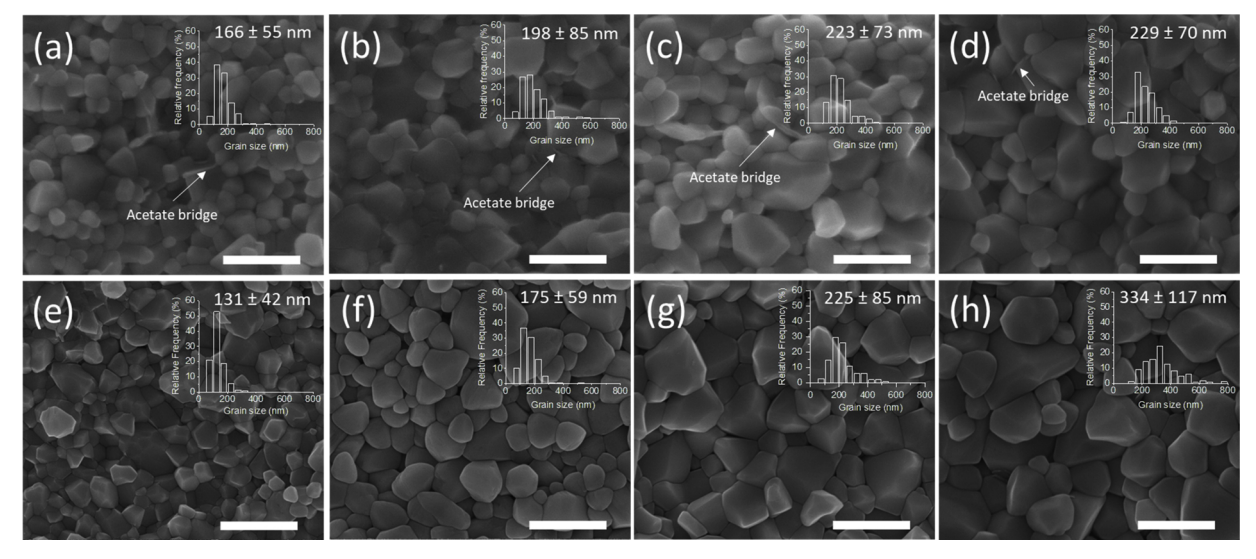


Fig. 6. HR-SEM images of (a)HS0, (b) HS20, (c) HS40, (d) HS80, (e) CSP0, (f) CSP20, (g) CSP40 and (h) CSP80. Grain size distribution and average grain sizes are inserted in the images. Scale bar: 500 nm.

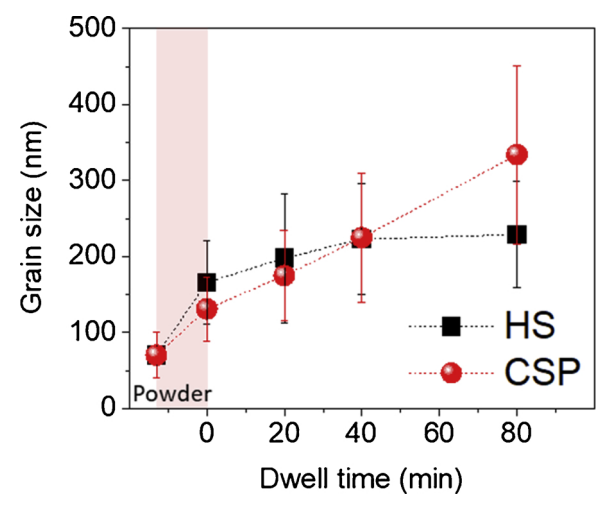


Fig. 7. Grain size evolution with the dwell time for HS and CSP. The red band corresponds to the heating. Dash lines must be considered as guide-to-the-eye. (For interpretation of the references to colour in this figure legend, the reader is referred to the web version of this article).

that correspond to CH_3COCH_3 and CH_3COO fragments, respectively. According to Moezzi et al., acetone (CH_3COCH_3) may be released from the decomposition of molten anhydrous zinc acetate following Eq. (5). Authors also observed the consumption of O_2 during the decomposition process to form CO_2 and H_2O [58], which is consistent with our analyses in Fig. 8e and f.

$$Zn(CH_3CO_2)_2 \rightarrow ZnO + CH_3COCH_3 + CO_2$$
 (5)

It is interesting to notice that amount of residual water and organics is almost constant in the case of CSP whatever the dwell time while it continuously decreases in the case of HS, which is consistent with Raman spectroscopy analysis (Fig. 5).

4. Discussion

4.1. Mechanical-chemical effects and relative density evolution

4.1.1. Mechanical-chemical effects

Analogous evolutionary trends (decrease and increase) and close values of relative density are observed for both hydrothermal and cold sintering (Fig. 3). This may be indicative of near-similar mechanical-chemical contributions for sintering techniques, mainly driven by pressure solution creep. The almost identical relative density of HSO and CSPO right after the heating ramp is of high importance as pressure solution creep was observed to be dominant in the first 10 min of thermal cycles in cold sintering [22,59]. This phenomenon takes place following chemical potential gradients from highly constrained areas ($\mu_{s,1}$), with enhanced dissolution and high chemical potential, to low constrained areas at particle surfaces with a lower chemical potential ($\mu_{s,2}$), through the liquid film separating particles. The driving force of pressure solution ($\Delta\mu_{tot}$) is therefore defined as (Eq. (6)): [60]

$$\Delta\mu_{tot} = \mu_{s,1} - \mu_{s,2} \tag{6}$$

The process is divided into three main steps (Fig. 9a): Dissolution, Mass transport and Precipitation. Gratier et al. [60] also assumed that the limiting steps in pressure solution will not affect its driving force presented at Eq. (6) (Supplementary Data, Fig. S 6) but will simply influence the rate at which it occurs.

• Dissolution:

The dissolution takes place following the chemical potential difference between the stressed solid $(\mu_{s,1})$ and the liquid phase in contact with it $(\mu_{l,1})$. The driving force for dissolution $(\Delta\mu_D)$ and is defined by Eq. (7):

$$\Delta \mu_D = \mu_{s,1} - \mu_{l,1} \tag{7}$$

Highly stressed grain contacts enhance the dissolution at the interface between the solid in contact with the liquid. Indeed, if one assumed that grains are spheres with a diameter d and are packed with a simple cubic packing; at a strain e_v , accumulated by postelastic creep, the grain-to-grain contacts becomes a circle with an area A_c (Fig. 9b). The stress intensification factor (B) is then defined by the Eq. (8): [61]

$$B = \frac{6d^2(1 - e_v)^{2/3}}{A_c} \tag{8}$$

The stress intensification factor is what makes the local pressure between two grains very high (up to several GPa) and what enhances dissolution at early stages of sintering [62], when the area A_c is small.

Mass transport

The mass transport takes place following the chemical potential

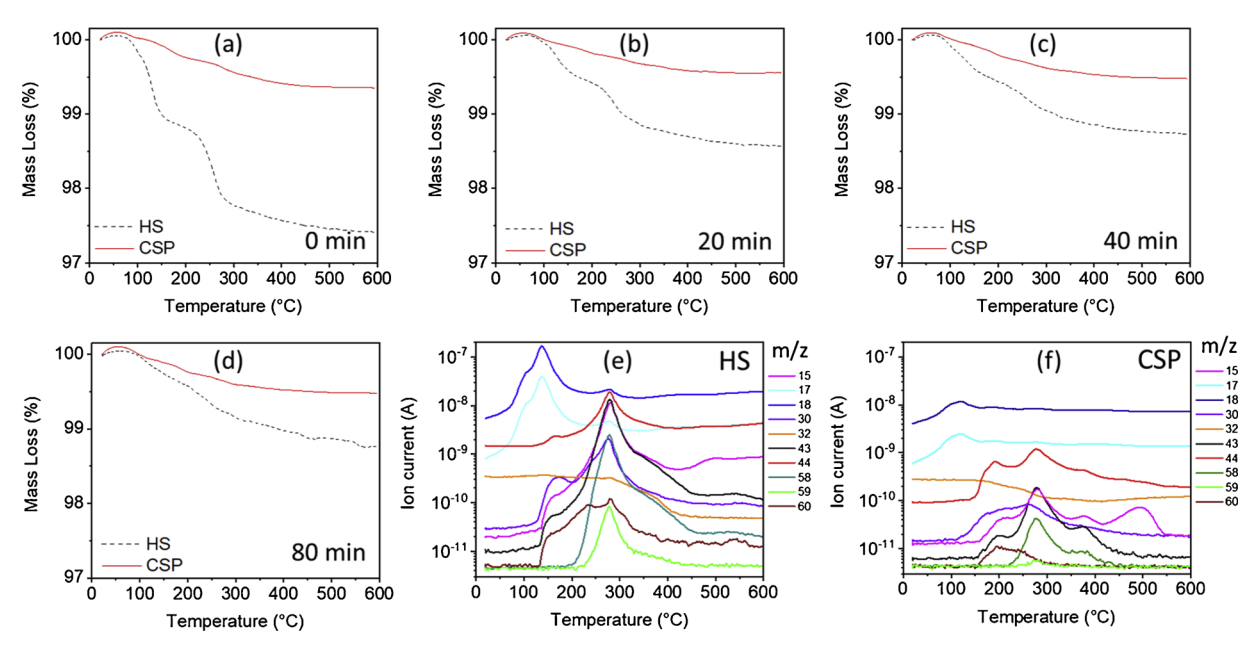


Fig. 8. TGA analysis of ZnO ceramics hydrothermally and cold sintered for (a) 0 min, (b) 20 min, (c) 40 min, (d) 80 min. Mass Spectroscopy of ZnO ceramics sintered for 40 min by (e) hydrothermal sintering and (f) cold sintering.

difference between the liquid phase with a high concentration of solute $(\mu_{l,1})$ and the liquid phase with a lower concentration of solute $(\mu_{l,2})$. The driving force for mass transport $(\Delta\mu_T)$ and is defined by Eq. (9):

$$\Delta \mu_T = \mu_{l,1} - \mu_{l,2} \tag{9}$$

According to Gratier et al. [60], the grain contact geometry, the texturation and model of grain boundaries, such as surface roughness resulting from the dissolution may influence the mass transport "realization" as well. These grain contact characteristics dynamically change during the pressure solution; fine interfacial structure of the grain boundaries will not be thoroughly investigated in this paper.

• Precipitation:

The precipitation takes place following the chemical potential difference between the liquid phase with a certain concentration of solute $(\mu_{l,2})$ and the less stressed solid, generally located at pore walls $(\mu_{s,2})$. The driving force for precipitation $(\Delta\mu_p)$ and is defined by Eq. (10):

$$\Delta \mu_P = \mu_{l,2} - \mu_{s,2} \tag{10}$$

The dissolution is the predominant factor at an early stage, which may explain why the average size is higher in HS. At following stages (dwell times of 20 min or higher), the presence of a higher amount of

solvent during the process due to the closed nature of the system leads to a lower kinetics to reach supersaturation and precipitation. In the meantime, during CSP, supersaturation considerably increases following evaporation, which may lead to larger grain sizes.

4.1.2. Relative density evolution

The decrease in relative density observed between 0 and 20 min or 40 min for CSP or HS, respectively, could be linked with the increase in pore size during the sintering. This phenomenon was already observed by Coble et al. [63] during the conventional sintering of ZnO. Kingery et al. reported that in conventional sintering, the pore growth occurs as a consequence of pore migration along with boundary migration, resulting in the coalescence of several pores [12,64]. Due to low sample volumes and high densities, mercury intrusion porosimetry analyses conducted on hydrothermally- and cold- sintered specimen did not allow to accurately study the evolution of the pore size distribution with the sintering time. However, after intrusion of mercury in different samples, it was noted that voids (cracks and pores) were mainly located at the rims of pellets (Supplementary Data, Fig. S 7).

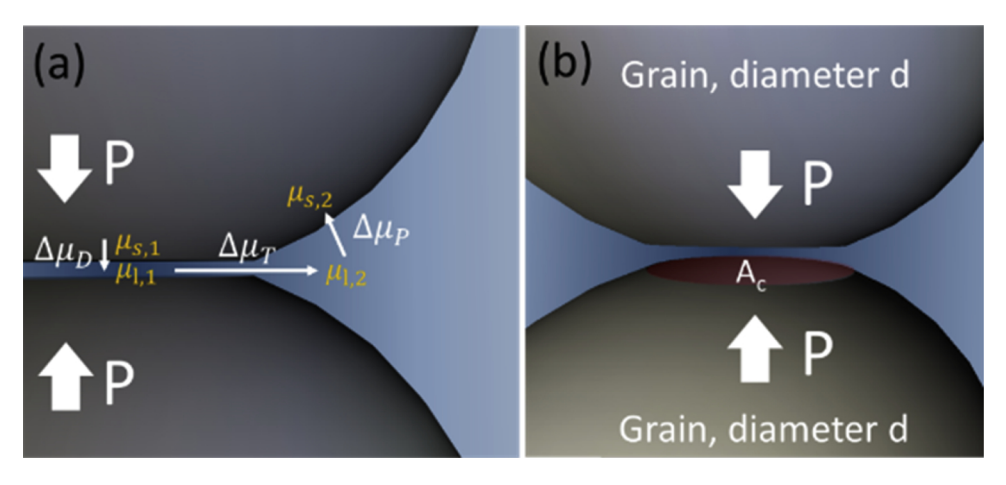


Fig. 9. (a) Three steps of the pressure solution creep: $\Delta\mu_D$, $\Delta\mu_T$ and $\Delta\mu_P$ are driving forces for dissolution, mass transport and precipitation, respectively. (b) Schematic of the model with two grains with a diameter d and a grain-tograin contact with an area A_c (in red). (For interpretation of the references to colour in this figure legend, the reader is referred to the web version of this article).

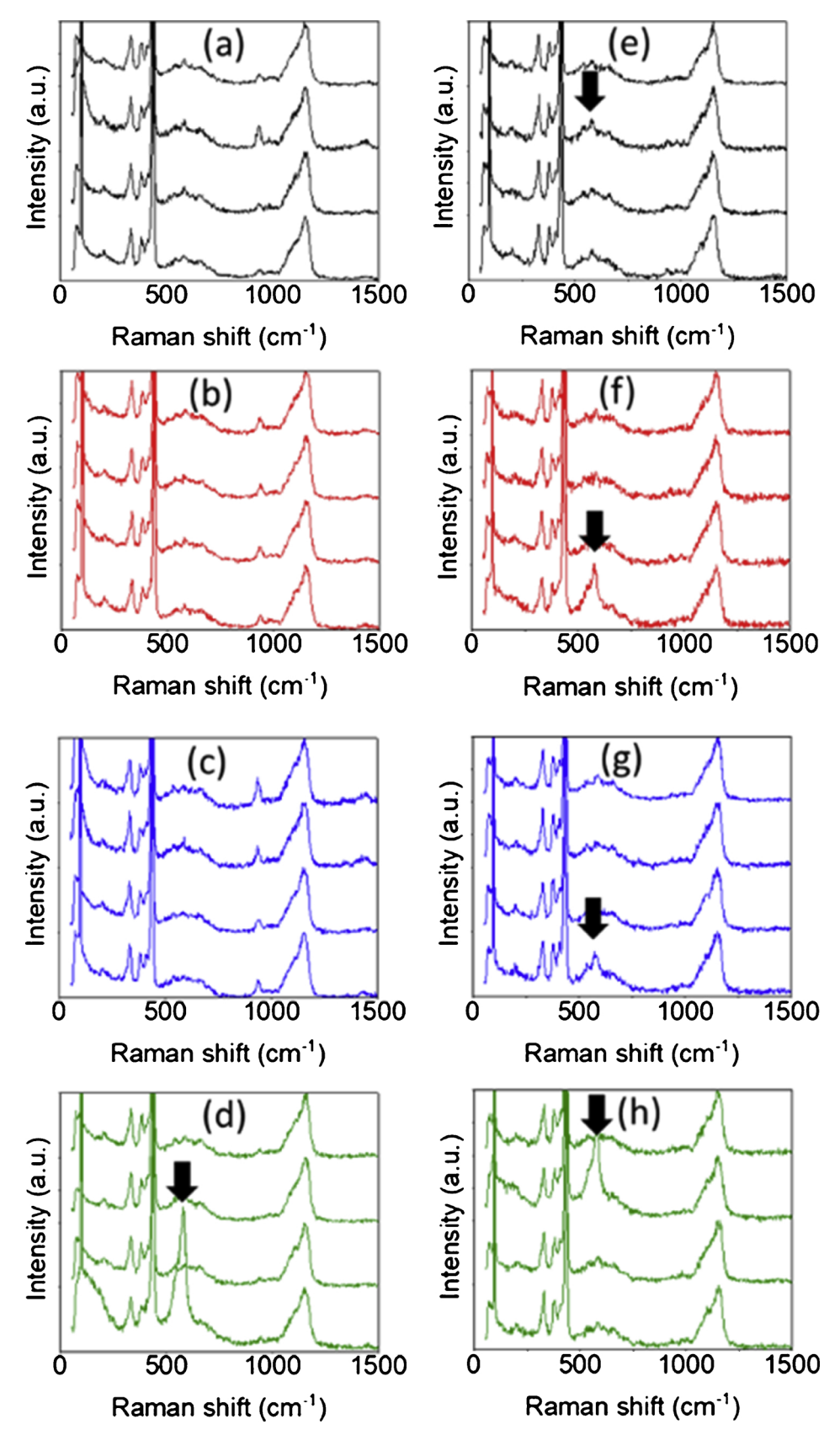


Fig. 10. Raman spectroscopy of hydrothermally sintered samples: (a) HS0, (b) HS20, (c) HS40, (d) HS80 and cold sintered samples: (e) CSP0, (f) CSP20, (g) CSP40, (h) CSP80.

4.2. Chemical effects

4.2.1. Grain size evolution

SEM analyses show a different grain size evolution between ZnO sintered by cold sintering (Fig. 6a–d) and hydrothermal sintering (Fig. 6e–h). Several reasons may explain it: the presence of oxygen vacancies, the grain boundary thickness and grain surface roughness, the presence of residual acetates at grain boundaries.

• Presence of oxygen vacancies

For each HS (Fig. 10a-d) and CSP (Fig. 10e-h) sample, Raman spectra were arbitrarily taken at four different points. A sharp E₁(LO) mode band, derived from the formation of oxygen vacancies, appears at $\sim 580\,\mathrm{cm}^{-1}$ in all the CSP samples, except for CSP0 where it is less sharp. On the other hand, no such a band was observed in the HS samples before 80 min. The origin of the oxygen vacancy formation could be associated with the acetate decomposition following interactions with the ZnO surface [41]. It is known that reducing gas is released during the decomposition of carboxylic acid that provides reducing atmosphere for adjacent ceramic grains [65]. TGA analyses in this study revealed that acetic acid decomposed at an earlier stage in CSP compared to HS. This may explain why oxygen vacancies formed earlier in CSP (Fig. 10). The higher oxygen vacancy concentration typically promotes the grain growth because it provides higher diffusivity [33]. The oxygen vacancy level is also critical for the grain boundary mobility that affects the grain growth [66].

These results suggest that, up to 80 min of dwell time, the formation of a more highly defective diffusion path through oxygen vacancies occurs during the CSP, promoting thus grain growth. Considering the spectrum relative to HS80, a reactivation of grain growth through defect formation cannot be discarded for longer dwell times in the case of HS.

• Grain boundary thickness and grain surface roughness

While comparing the Fig. 11a and d, one may assume that grain interfaces of HS samples are rougher than the CSP ones. Besides, the grain boundary thickness is globally higher for hydrothermal sintering than cold sintering, following the amount of the remaining solvent confined to a more advanced stage of HS compared to CSP. This may have an influence on the overall kinetics of low temperature sintering as well as grain growth. Even if it is beyond the scope of this paper, tailoring the thickness and the chemistry of grain boundaries thanks to suitable conditions of low sintering temperature process could be a promising option considering the distinctive microstructure of ZnO based varistors with complex chemistry of grains boundaries forming potential barriers.

• Presence of residual acetates at grain boundaries

TG-MS analysis confirmed that hydrothermally sintered samples contain more residual acetates than cold sintered samples (Fig. 8). STEM-EDS images presented in Fig. 11b and e, show that residual acetates are mainly located in the pores trapped at the triple junctions for cold sintered samples; and located in both the pores and at some grain boundaries for hydrothermally sintered samples.

Even though the final density values of the sintered pellets are quasi-similar (Fig. 2), the grain growth kinetics of cold sintered samples is relatively higher than the hydrothermally sintered ones, except during the heating (Fig. 7). Sengul et al. [67] unveiled an accelerated surface diffusion mechanism that can be activated during cold sintering processes, and can also be activated during hydrothermal-sintering. This mechanism can be hindered by the presence of residual molecules in the system. These molecules can be adsorbed on the surface and, when in excess, can create barriers whose energy is higher than the

driving force for surface diffusion and in turn, prevent from grain growth. Besides, as discussed above, the cold sintering process is conducted in an open system, thus, the liquid is removed from the system earlier than hydrothermal sintering. As a result, the accelerated surface diffusion mechanism in cold sintering process is less likely to be affected by the surface complexations compared to hydrothermal sintering.

4.2.2. Zinc acetate "bridge" formation: ReaxFF molecular dynamics simulations

In order to investigate the difference between cold sintering process (CSP) and hydrothermal sintering (HS) at the atomistic level, we conducted ReaxFF molecular dynamics (MD) simulations [68,69]. The ReaxFF is a reactive force field which is capable of modeling sub and supercritical conditions in reactive liquid/solid interfaces [41,42]. The simulated molecular systems for both CSP and HS are composed of ZnO (10 $\bar{1}$ 0) surface, solvent and Zn²+ ions, and the solvent is water and acetic acid mixture. In order to capture the difference between the two sintering processes, the solvent in CSP system is kept in a gaseous state while HS system is kept in subcritical conditions as suggested by Goglio et al. [12]. Refer to the computational methods section for details.

At room temperature, the interaction between the solvent and the ZnO surface results in the formation of a hydroxide layer due to dissociation of water and acetic acid molecules on surface ions. Above the hydroxide layer, a tightly bound solvent layer is formed due to the interactions between the solvent molecules and the hydroxide layer. According to MD simulations conducted in this study, the difference between CSP and HS results in a distinctive chemical activity in the system. In CSP, the transition from liquid to gaseous state results in the removal of the tightly bound solvent layer from the surface. The removal of this layer makes the surface easily accessible by precipitated ions, and thus favors the interactions between the surface and Zn2+ ions. As a result, the process is dominated by surface kinetics. However, in HS, the increase in temperature while keeping the solvent in the system creates a hydrothermally active layer on the surface. The presence of the hydrothermal layer results in the formation of metal-organic complexes (Fig. 12B) that are composed of zinc atoms connected by acetate molecules (zinc acetate chains). In order to investigate the role of the zinc acetate chains further, we conducted separate simulations at hydrothermal conditions for more extended time scales (see computational methods section for details). According to our simulations, the zinc-acetate chains initiate zinc-acetate clusters. The zinc-zinc pair distribution functions (PDFs) for HS simulations at temperature 300 K and 500 K are given in Fig. 12A. As can be seen from the PDFs, when the hydrothermal conditions are established at 500 K, a peak around 4 Å is formed. This peak represents the distance between Zn²⁺ ions in zinc-acetate clusters (Fig. 12B). By assuming that the zincacetate clusters are converted into zinc-acetate crystals in longer timescale, it is safe to say that this finding is consistent with the experimental X-ray characterization of densified ceramics.

5. Conclusion

We investigated the similarities and differences between the cold sintering process (CSP) and the hydrothermal sintering (HS), in the case of zinc oxide (ZnO). Materials were sintered at $155\pm5\,^{\circ}\mathrm{C}$ with a pressure of 320 MPa, and different dwell times (0 min, 20 min, 40 min and 80 min). Very high relative densities were reached using both processes. CSP and HS are based on the low temperature sintering of materials in the presence of a transient liquid and uniaxial pressure, in open conditions for the cold sintering process and in closed conditions for the hydrothermal sintering. Both processes shown analogous evolutionary trends and close values of relative density, which may indicate a near-similar mechanical-chemical contributions, governed by the pressure solution creep. The different grain size evolution observed between both processes may originate from the presence of oxygen

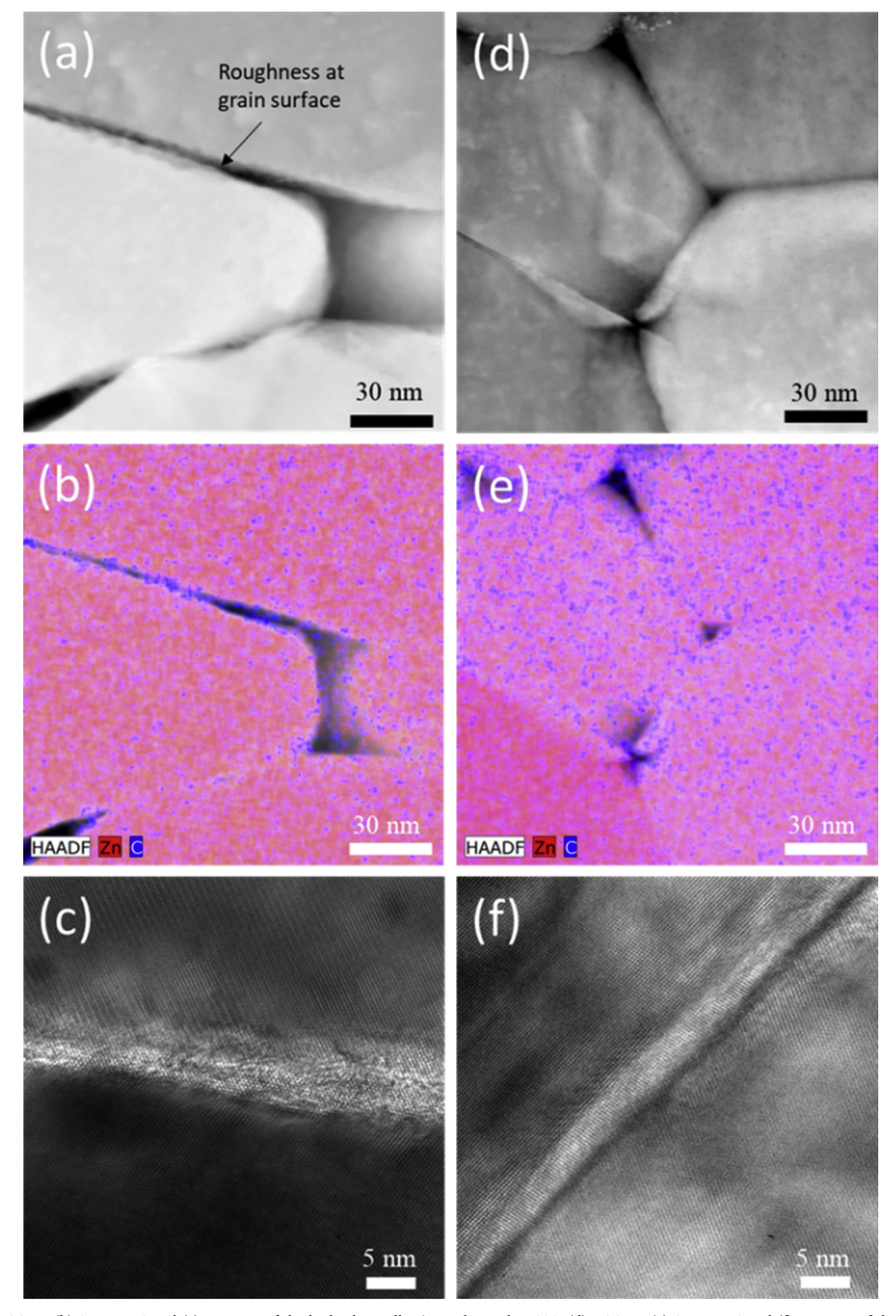
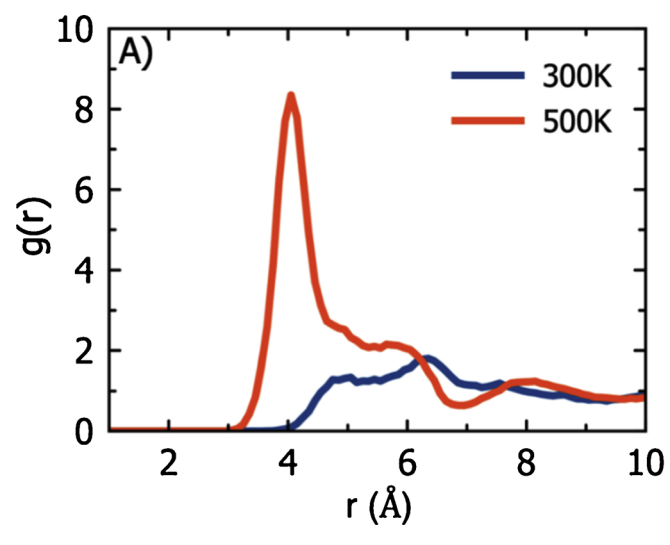


Fig. 11. (a) HAADF, (b) STEM-EDS and (c) HR TEM of the hydrothermally sintered sample HS80; (d) HAADF, (e) STEM-EDS and (f) HR TEM of the cold sintered sample CSP80.



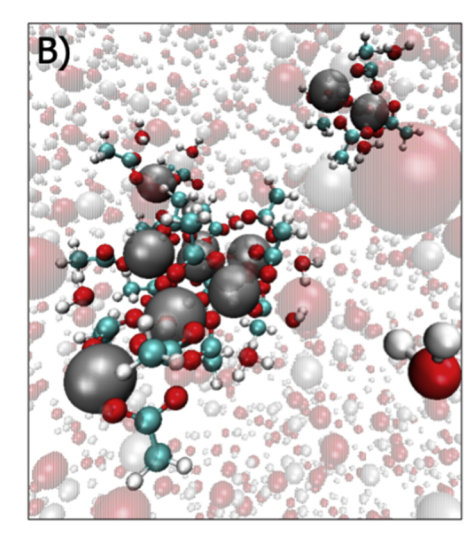


Fig. 12. (A) The zinc-zinc pair distribution functions (PDFs) of the solvent in Hydrothermal Sintering system at different temperatures. Clustering of zinc atoms can be seen from the transition from wide distance distribution (blue line) to a sharp peak (red line). The distance between two zinc atoms in zinc-acetate is approximately 4.0 Å. (B) Visualization of zinc-acetate cluster and metal-organic complex obtained by ReaxFF MD simulations. Key: Zn²⁺ ion (grey), Oxygen atom (red), Hydrogen atom (white), Carbon atom (cyan). (For interpretation of the references to colour in this figure legend, the reader is referred to the web version of this article).

vacancies, grain boundary thickness, grain surface roughness and the presence of residual acetates at grain boundaries.

These features were characterized individually by different methods but, no quantitative analysis was made to determine the respective weight of their contribution to the grain size evolution. However, the "residence time" and the state of the residual solvent within the ceramic were shown as key parameters in terms of surface reactivity and grain boundaries characteristics. This represents the major difference between the two open and closed systems and is well illustrated by the formation and impact of zinc acetate "bridges". By combining ReaxFF MD simulations and experiments to investigate the formation of zinc acetate "bridges", we were able to observe that CSP and HS differ in their chemical activities. Indeed, the solvent evaporation in CSP removes the tightly bound solvent layer from the surface and aids the interaction between the surface and Zn²⁺ ions, while that tightly bound solvent layer stays active in hydrothermal sintering, resulting in the formation of connected metal-organic complexes. They lead to zinc acetate clusters, converted into zinc acetate crystals (detectable by XRD and SEM) in a longer timescale.

Declaration of Competing Interest

The authors declare that they have no known competing financial interests or personal relationships that could have appeared to influence the work reported in this paper.

Acknowledgment

This work was supported by Murata Manufacturing Co., Ltd (funding 432-43 42MM, A.N.), the National Science Foundation (DMR-1728634) and AFOSR grant (grant no. FA9550-16-1-0429, C.A.R.). A.C.T.vD acknowledges funding support from the Multi-Scale Fluid-Solid Interactions in Architected and Natural Materials (MUSE) Center funded by U.S. Department of Energy (DOE). MYS acknowledges partial funding support from U.S. National Science Foundation under Award No. DMR-1842922. We gratefully acknowledge Dr. Ke Wang (Materials Characterization Laboratory, Penn State University) for TEM analysis and Dr. Marie-Anne Dourges (Institut des Sciences Moléculaires, UMR 5255) for mercury intrusion porosimetry and fruitful discussions.

Appendix A. Supplementary data

Supplementary material related to this article can be found, in the online version, at doi:https://doi.org/10.1016/j.jeurceramsoc.2019.11. 049.

References

- D.M. Roy, G.R. Gouda, A. Bobrowsky, Very high strength cement pastes prepared by hot pressing and other high pressure techniques, Cem. Concr. Res. 2 (1972) 349–366.
- [2] D.M. Roy, G. Gouda, High strength generation in cement pastes, Cem. Concr. Res. 3 (1973) 807–820.
- [3] H. Toraya, M. Yoshimura, S. Sōmiya, Hydrothermal reaction sintering of monoclinic HfO₂, J. Am. Ceram. Soc. 65 (1982) c159–c160, https://doi.org/10.1111/j. 1151-2916.1982.tb10527.x.
- [4] S.-I. Hirano, S. Sōmiya, Hydrothermal reaction sintering of pure Cr₂O₃, J. Am. Ceram. Soc. 59 (1976) 534, https://doi.org/10.1111/j.1151-2916.1976.tb09432.x.
- [5] N. Yamasaki, K. Yanagisawa, M. Nishioka, S. Kanahara, A hydrothermal hotpressing method: apparatus and application, J. Mater. Sci. Lett. 5 (1986) 355–356, https://doi.org/10.1007/BF01748104.
- [6] Y. Xie, S. Yin, H. Yamane, T. Hashimoto, T. Sato, Low temperature sintering and color of a new compound Sn_{1.24}Ti_{1.94}O_{3.66}(OH)_{1.50}F_{1.42}, Solid State Sci. 11 (2009) 1703–1708, https://doi.org/10.1016/j.solidstatesciences.2009.05.025.
- [7] N. Yamasaki, T. Weiping, K. Jiajun, Low-temperature sintering of calcium carbonate by a hydrothermal hot-pressing technique, J. Mater. Sci. Lett. 11 (1992) 934–936.
- [8] N. Yamasaki, T. Kai, M. Nishioka, K. Yanagisawa, K. Ioku, Porous hydroxyapatite ceramics prepared by hydrothermal hot pressing, J. Mater. Sci. Lett. 9 (1990) 1150.
- [9] K. Yanagisawa, M. Nishioka, K. Ioku, N. Yamasaki, Neck formation of spherical silica particles by hydrothermal hot pressing, J. Mater. Sci. Lett. 9 (1990) 7–8, https://doi.org/10.1007/BF00724415.
- [10] S. Katsuyama, Y. Takiguchi, M. Ito, Synthesis of Ca₃Co₄O₉ ceramics by citric acid complex and hydrothermal hot-pressing processes and investigation of its thermoelectric properties, Mater. Trans. 48 (2007) 2073–2078, https://doi.org/10.2320/matertrans.E-MRA2007805.
- [11] G. Goglio, A. Largeteau, A. Ndayishimiye, M. Prakasam, Procédé et dispositif de densification des matériaux ou de consolidation d'un assemblage de matériaux par frittage hydrothermal ou solvothermal. Patent WO 2018/215559. 2018.
- [12] G. Goglio, A. Ndayishimiye, A. Largeteau, C. Elissalde, View point on hydrothermal sintering: main features, today's recent advances and tomorrow's promises, Scr. Mater. 158 (2019) 146–152, https://doi.org/10.1016/j.scriptamat.2018.08.038.
- [13] A. Ndayishimiye, A. Largeteau, S. Mornet, M. Duttine, M.-A. Dourges, D. Denux, M. Verdier, M. Gouné, T.H. de Beauvoir, C. Elissalde, G. Goglio, Hydrothermal sintering for densification of silica. Evidence for the role of water, J. Eur. Ceram. Soc. (2017), https://doi.org/10.1016/j.jeurceramsoc.2017.10.011.
- [14] A. Ndayishimiye, S. Buffière, M.A. Dourges, A. Largeteau, M. Prakasam, S. Mornet, O. Kaman, J. Zdeněk, J. Hejtmánek, G. Goglio, Design of 0–3 type nanocomposites using hydrothermal sintering, Scr. Mater. 148 (2018) 15–19, https://doi.org/10. 1016/j.scriptamat.2018.01.013.
- [15] O. Kaman, Z. Jirak, J. Hejtmánek, A. Ndayishimiye, M. Prakasam, G. Goglio,

- Tunneling magnetoresistance of hydrothermally sintered $La_{1,x}Sr_xMnO_3$ -silica nanocomposites.pdf, J. Magn. Magn. Mater. 479 (2019) 135–143.
- [16] R.E. Riman, V. Atakan, Method of Hydrothermal Liquid Phase Sintering of Ceramic Materials and Products Devired Therefrom, US Patent 8,313,802 (2012) and 8,709, 960 (2014), n.d.
- [17] C. Vakifahmetoglu, J.F. Anger, V. Atakan, S. Quinn, S. Gupta, Q. Li, L. Tang, R.E. Riman, Reactive hydrothermal liquid-phase densification (rHLPD) of Ceramics. A study of the BaTiO₃[TiO₂] composite system, J. Am. Ceram. Soc. 99 (2016) 3893–3901, https://doi.org/10.1111/jace.14468.
- [18] Q. Li, S. Gupta, L. Tang, S. Quinn, V. Atakan, R.E. Riman, A novel strategy for carbon capture and sequestration by rHLPD Processing, Front. Energy Res. 3 (2016) 1–11, https://doi.org/10.3389/fenrg.2015.00053.
- [19] H. Guo, A. Baker, J. Guo, C.A. Randall, Protocol for ultralow-temperature ceramic sintering: an integration of nanotechnology and the cold sintering process, ACS Nano 10 (2016) 10606–10614, https://doi.org/10.1021/acsnano.6b03800.
- [20] J. Guo, H. Guo, A.L. Baker, M.T. Lanagan, E.R. Kupp, G.L. Messing, C.A. Randall, Cold sintering: a paradigm shift for processing and integration of ceramics, Angew. Chemie - Int. Ed. 55 (2016) 11457–11461, https://doi.org/10.1002/anie. 2016.5442
- [21] H. Guo, J. Guo, A. Baker, C.A. Randall, Hydrothermal-assisted cold sintering process: a new guidance for low-temperature ceramic sintering, ACS Appl. Mater. Interfaces 8 (2016) 20909–20915, https://doi.org/10.1021/acsami.6b07481.
- [22] F. Bouville, A.R. Studart, Geologically-inspired strong bulk ceramics made with water at room temperature, Nat. Commun. 8 (2017) 14655, https://doi.org/10. 1038/ncomms14655.
- [23] J. Guo, R. Floyd, S. Lowum, J. Maria, T. Herisson De Beauvoir, J.-H. Seo, C.A. Randall, Cold sintering: progress, challenges, and future opportunities, Annu. Rev. Mater. Res. 49 (2019) 275–295.
- [24] J.P. Maria, X. Kang, R.D. Floyd, E.C. Dickey, H. Guo, J. Guo, A. Baker, S. Funihashi, C.A. Randall, Cold sintering: current status and prospects, J. Mater. Res. 32 (2017) 3205–3218, https://doi.org/10.1557/jmr.2017.262.
- [25] A. Baker, H. Guo, J. Guo, C. Randall, Utilizing the cold sintering process for flexible-printable electroceramic device fabrication, J. Am. Ceram. Soc. 3 (2016) 1–3, https://doi.org/10.1111/jace.14467.
- [26] H. Kähäri, M. Teirikangas, J. Juuti, H. Jantunen, Dielectric properties of lithium molybdate ceramic fabricated at room temperature, J. Am. Ceram. Soc. 97 (2014) 3378–3379, https://doi.org/10.1111/jace.13277.
- [27] J. Guo, S.S. Berbano, H. Guo, A.L. Baker, M.T. Lanagan, C.A. Randall, Cold sintering process of composites: bridging the processing temperature gap of ceramic and polymer materials, Adv. Funct. Mater. 26 (2016) 7115–7121, https://doi.org/10. 1002/adfm.201602489.
- [28] C. Elissalde, U. Chung, M. Josse, G. Goglio, M.R. Suchomel, J. Majimel, A. Weibel, F. Soubie, A. Flaureau, A. Fregeac, C. Estournès, Single-step sintering of zirconia ceramics using hydroxide precursors and spark plasma sintering below 400 ° C, Scr. Mater. 168 (2019) 134–138, https://doi.org/10.1016/j.scriptamat.2019.04.037.
- [29] T.H. De Beauvoir, A. Sangregorio, A. Bertrand, C. Payen, D. Michau, U. Chung, Cool-SPS stabilization and sintering of thermally fragile, potentially magnetoelectric, NH 4FeP2O7, Ceram. Int. 45 (2019) 9674–9678, https://doi.org/10.1016/ i.ceramint.2018.12.103.
- [30] T.H. De Beauvoir, A. Sangregorio, I. Cornu, C. Elissalde, M. Josse, Cool-SPS: an opportunity for low temperature sintering of thermodynamically fragile materials, J. Mater. Chem. C 6 (2018) 2229–2233, https://doi.org/10.1039/c7tc05640k.
- [31] Ü. Özgür, Y.I. Alivov, C. Liu, A. Teke, M.A. Reshchikov, S. Do, V. Avrutin, A comprehensive review of ZnO materials and devices, J. Appl. Phys. 98 (2005) 041301, https://doi.org/10.1063/1.1992666.
- [32] S. Funahashi, J. Guo, H. Guo, K. Wang, A.L. Baker, K. Shiratsuyu, C.A. Randall, Demonstration of the cold sintering process study for the densification and grain growth of ZnO ceramics, J. Am. Ceram. Soc. 6 (2016) 1–6, https://doi.org/10. 1111/jace.14617.
- [33] T.K. Gupta, R.L. Coble, Sintering of ZnO: I, densification and grain growth, J. Am. Ceram. Soc. 51 (1968) 521–525.
- [34] J. Langer, M.J. Hoffmann, O. Guillon, Electric field-assisted sintering and hot pressing of semiconductive, J. Am. Ceram. Soc. 94 (2011) 2344–2353, https://doi. org/10.1111/j.1551-2916.2011.04396.x.
- [35] J. Gonzalez-Julian, K. Neuhaus, M. Bernemann, J. Pereira da Silva, A. Laptev, M. Bram, O. Guillon, Unveiling the mechanisms of cold sintering of ZnO at 250°C by varying applied stress and characterizing grain boundaries by Kelvin Probe Force Microscopy, Acta Mater. 144 (2018) 116–128, https://doi.org/10.1016/j.actamat. 2017.10.055.
- [36] X. Kang, R. Floyd, S. Lowum, M. Cabral, E. Dickey, J.-P. Maria, Mechanism studies of hydrothermal cold sintering of zinc oxide at near room temperature, J. Am. Ceram. Soc. 102 (2019) 4459–4469, https://doi.org/10.1111/jace.16340.
- [37] T. Roisnel, J. Rodriquez-Carvajal, WinPLOTR: a windows tool for powder diffraction pattern analysis, Eur. Powder Diffr. EPDIC 7, Trans Tech Publications Ltd, 2001, pp. 118–123 doi:10.4028/www.scientific.net/MSF.378-381.118.
- [38] C.A. Schneider, W.S. Rasband, K.W. Eliceiri, NIH Image to ImageJ: 25 years of image analysis, Nat. Methods 9 (2012) 671–675, https://doi.org/10.1038/nmeth.
- [39] A. Wander, N.M. Harrison, An ab initio study of ZnO (10-10), Surf. Sci. 457 (2000) L342–L346.
- [40] B. Ludi, M. Niederberger, Zinc oxide nanoparticles: chemical mechanisms and classical and non-classical crystallization, Dalton Trans. 42 (2013) 12554–12568, https://doi.org/10.1039/c3dt50610j.
- [41] M.Y. Sengul, C.A. Randall, A.C.T. Van Duin, ReaxFF molecular dynamics study on the influence of temperature on adsorption, desorption, and decomposition at the acetic acid / water / ZnO (101⁻0) interface enabling cold sintering, ACS Appl.

- Mater. Interfaces 10 (2018) 37717–37724, https://doi.org/10.1021/acsami. 8b13630.
- [42] M.Y. Sengul, C.A. Randall, A.C.T. Van Duin, ReaxFF molecular dynamics simulation of intermolecular structure formation in acetic acid-water mixtures at elevated temperatures and pressures, J. Chem. Phys. 148 (2018) 164506, https://doi.org/10. 1063/1.5025932.
- [43] E.J. Baerends, T. Ziegler, A.J. Atkins, J. Autschbach, D. Bashford, O. Baseggio, A. Bérces, F.M. Bickelhaupt, C. Bo, P.M. Boerritger, L. Cavallo, C. Daul, D.P. Chong, D.V. Chulhai, L. Deng, R.M. Dickson, J.M. Dieterich, D.E. Ellis, M. van Faassen, A. Ghysels, A. Giammona, S.J.A. van Gisbergen, A. Goez, A.W. Gtz, S. Gusarov, F.E. Harris, P. van den Hoek, Z. Hu, C.R. Jacob, H. Jacobsen, L. Jensen, L. Joubert, J.W. Kaminski, G. van Kessel, C. Knig, F. Kootstra, A. Kovalenko, M. Krykunov, E. van Lenthe, D.A. McCormack, A. Michalak, M. Mitoraj, S.M. Morton, J. Neugebauer, V.P. Nicu, L. Noodleman, V.P. Osinga, S. Patchkovskii, M. Pavanello, C.A. Peeples, P.H.T. Philipsen, C.C. Post, D. Pye, H. Ramanantoanina, P. Ramos, W. Ravenek, J.I. Rodrguez, P. Ros, R. Rger, P.R.T. Schipper, D. Schlns, H. van Schoot, G. Schreckenbach, J.S. Seldenthuis, M. Seth, J.G. Snijders, Theoretical Chemistry, ADF2017; SCM, Vrije Universiteit, Amsterdam, Amsterdam, The Netherlands, 2017.
- [44] H.J. Berendsen, J.P. Postma, W.F. van Gunsteren, A. Di Nola, J.R. Haak, Molecular dynamics with coupling to an external bath, J. Chem. Phys. 81 (1984) 3684–3690, https://doi.org/10.1063/1.448118.
- [45] E.H. Kisi, M.M. Elcombe, u Parameters for the wurtzite structure of ZnS and ZnO using powder neutron diffraction, Acta Crystallogr. C45 (1989) 1867–1870, https://doi.org/10.1107/S0108270189004269.
- [46] H. Schulz, K.H. Thiemann, Structure parameters and polarity of the Wurtzite type compounds SiC—2H and ZnO, Solid State Commun. 32 (1979) 783–785.
- [47] Y. Zhang, F. Zhu, J. Zhang, L. Xia, Converting layered zinc acetate nanobelts to onedimensional structured ZnO nanoparticle aggregates and their photocatalytic activity, Nanoscale Res. Lett. 3 (2008) 201–204, https://doi.org/10.1007/s11671-008-9136-2.
- [48] A. Tarat, C.J. Nettle, D.T.J. Bryant, D.R. Jones, M.W. Penny, R.A. Brown, R. Majitha, K.E. Meissner, T.G.G. Maffeis, Microwave-assisted synthesis of layered basic zinc acetate nanosheets and their thermal decomposition into nanocrystalline ZnO, Nanoscale Res. Lett. 9 (2014) 1–8.
- [49] C.A. Arguello, D.L. Rousseau, S.P.S. Porto, First-order Raman effect in Wurtzite-type crystals, Phys. Rev. 181 (1969) 1351–1363.
- [50] Z.Q. Chen, A. Kawasuso, Y. Xu, H. Naramoto, Production and recovery of defects in phosphorus-implanted ZnO, J. Appl. Phys. 97 (2005) 013528, https://doi.org/10. 1063/1.1821636 1-6.
- [51] R. Zhang, P. Yin, N. Wang, L. Guo, Photoluminescence and Raman scattering of ZnO nanorods, Solid State Sci. 11 (2009) 865–869, https://doi.org/10.1016/j.solidstatesciences.2008.10.016.
- [52] R. Cuscó, E. Alarcón-lladó, J. Ibáñez, L. Artús, J. Jiménez, B. Wang, M.J. Callahan, Temperature dependence of Raman scattering in ZnO, Phys. Rev. B 75 (2007) 165202, https://doi.org/10.1103/PhysRevB.75.165202.
- [53] M.M. Yang, D.A. Crerar, D.E. Irish, A Raman spectroscopic study of lead and zinc acetate complexes in hydrothermal solutions, Geochemica Cosmochem. Acta. 53 (1989) 319–326.
- [54] M. Nagao, On Physisorption of Water on zinc oxide surface, J. Phys. Chem. 75 (1971) 3822–3828, https://doi.org/10.1021/j100694a007.
- [55] M.F. Khan, A.H. Ansari, M. Hameedullah, E. Ahmad, F. Mabood Husein, Q. Zia, U. Baig, M.R. Zaheer, M.M. Alam, A.M. Khan, Z.A. Alothman, I. Ahmad, G.M. Ashraf, G. Aliev, Sol-gel synthesis of thorn-like ZnO nanoparticles endorsing mechanical stirring effect and their antimicrobial activities: Potential role as nanoantibiotics, Sci. Rep. 6 (2016) 27689, https://doi.org/10.1038/srep27689.
- [56] T. Arii, A. Kishi, The effect of humidity on thermal process of zinc acetate, Thermochim. Acta 400 (2003) 175–185.
- [57] H. Yoneyama, Y. Takao, H. Tamura, A.J. Bard, Factors influencing product distribution in photocatalytic decomposition ofaqueous acetic acid on platanized TiO₂, J. Phys. Chem. 87 (1983) 1417–1422, https://doi.org/10.1021/j100231a027.
- [58] A. Moezzi, A. Mcdonagh, A. Dowd, M. Cortie, Zinc hydroxyacetate and its transformation to nanocrystalline zinc oxide, Inorg. Chem. 52 (2013) 95–102, https://doi.org/10.1021/ic302328e.
- [59] A. Ndayishimiye, K. Tsuji, K. Wang, S.H. Bang, C.A. Randall, Sintering mechanisms and dielectric properties of cold sintered (1-x) SiO₂ - x PTFE composites, J. Eur. Ceram. Soc. 39 (2019) 4743–4751, https://doi.org/10.1016/j.jeurceramsoc.2019. 07.048.
- [60] J.-P. Gratier, D.K. Dysthe, F. Renard, The role of pressure solution creep in the ductility of the Earth's upper crust, Adv. Geophys. 54 (2013) 47–179.
- [61] X. Zhang, C.J. Spiers, C.J. Peach, Compaction creep of wet granular calcite by pressure solution at 28°C to 150°C, J. Geophys. Res. 115 (2010) B09217, https:// doi.org/10.1029/2008JB005853 1–18.
- [62] S.H. Bang, A. Ndayishimiye, C.A. Randall, Mechanistic approach to identify densification kinetics and mechanisms of zinc oxide cold sintering, Acta Mater. (n.d.). doi:https://ssrn.com/abstract=3428070.
- [63] T.K. Gupta, R.L. Coble, Sintering of ZnO: II, density decrease and pore growth during the final stage of the process, J. Am. Ceram. Soc. 51 (1968) 525–528.
- [64] W.D. Kingery, B. François, Grain growth in porous compacts, J. Am. Ceram. Soc. Discuss. Notes. 48 (1965) 546–547.
- [65] D.C. Sinclair, A.R. West, Effect of atmosphere on the PTCR properties of BaTiO₃ ceramics, J. Mater. Sci. 29 (1994) 6061–6068.
- [66] W. Rheinheimer, J.P. Parras, J.-H. Preusker, R.A. De Souza, M.J. Hoffmann, Grain growth in strontium titanate in electric fields: The impact of space-charge on the grain-boundary mobility, J. Am. Ceram. Soc. 102 (2019) 3779–3790, https://doi. org/10.1111/jace.16217.

- [67] M.Y. Sengul, J. Guo, C.A. Randall, A.C.T. Van Duin, Water-mediated surface diffusion mechanism enabling the Cold Sintering Process: A combined computational and experimental study, Angew. Chemie Int. Ed. (n.d.). doi:10.1002/ange. 201904738.
- [68] A.C.T. Van Duin, S. Dasgupta, F. Lorant, W.A. Goddard III, ReaxFF: a reactive force field for hydrocarbons, J. Phys. Chem. A 105 (2001) 9396–9409, https://doi.org/
- 10.1021/jp004368u.
- [69] T.P. Senftle, S. Hong, M. Islam, S.B. Kylasa, Y. Zheng, Y.K. Shin, C. Junkermeier, R. Engel-herbert, M.J. Janik, H.M. Aktulga, T. Verstraelen, A. Grama, A.C.T. Van Duin, The ReaxFF reactive force-field: development, applications and future directions, Npj Comput. Mater. 15011 (2016) 1–14, https://doi.org/10.1038/npjcompumats.2015.11.